Source of correlated atom pairs

Here we develop two experimental techniques for producing *s*-wave scattering halos as a source of correlated atom pairs. First method utilises Bragg diffraction to split BEC into two clouds of different velocities, which produces a single *s*-wave halo. This method is very similar to the original demonstration by Perrin, *et al* [36]. The second method we demonstrate here, is a novel extension of this technique to the Kapitza-Dirac regime which allows for many (>10) diffraction orders to collide, with adjacent orders producing several distinct *s*-wave halos.

Initially, the BEC is prepared and trapped in the magnetically sensitive sublevel $m_J = +1$. The atomic clouds in this state are affected by stray magnetic field gradients and by the magnetic trap switch-off. This leads to substantial distortions in the reconstructed atomic positions on the detector. To overcome this disadvantage, as a first step in the experimental sequence, we transfer the atoms to a magnetically insensitive $m_J = 0$ state by employing Raman transition. This step outcouples atoms from the magnetic trap. The actual collision leading to an *s*-wave scattering is then achieved by splitting the BEC into the different momentum states via Bragg or Kapitza-Dirac diffraction.

Section 2.4 gives an introduction to the Raman and Bragg scattering and their application to quantum control, – the two-photon processes which are instrumental for the experiments described in this chapter. Generation and the key properties of the *s*-wave scattering halo is given in Section 2.6.

5.1   Raman and Bragg transitions

Here we describe the techniques and protocols developed to drive stimulated Raman and Bragg transitions in our $^4\mathrm{He}^*$BEC experiment. We begin with preparation and the geometry of the laser beams and then discuss design of the waveforms and pulse sequences.

5.1.1   Laser beams

The principal optical layout for the Bragg/Raman laser beams is shown in Fig. 5.1. Setup utilises the 1083 nm Yb^{3+} fiber laser (IRE Polus/IPG Photonics) with the maximum output power of 1 W. The first acoustic-optic modulator $\mathrm{AOM_{N.E.}}$ (Crystal Technology-???) forms a part of the intensity stabilisation block ("noise eater"), with the photodiode (PD) and PID controller forming a feedback loop; the intensity set-point for the PID is $I_0^{\mathrm{N.E.}}$. The lock cancels out the inherent intensity noise of the laser output to <1% within the bandwith of at least ∼100 kHz. $\mathrm{AOM_{N.E.}}$ has acoustic diffraction efficiency of ∼80% and operates in the "−1" diffraction order. Portion of the "0"-order beam is fiber-coupled
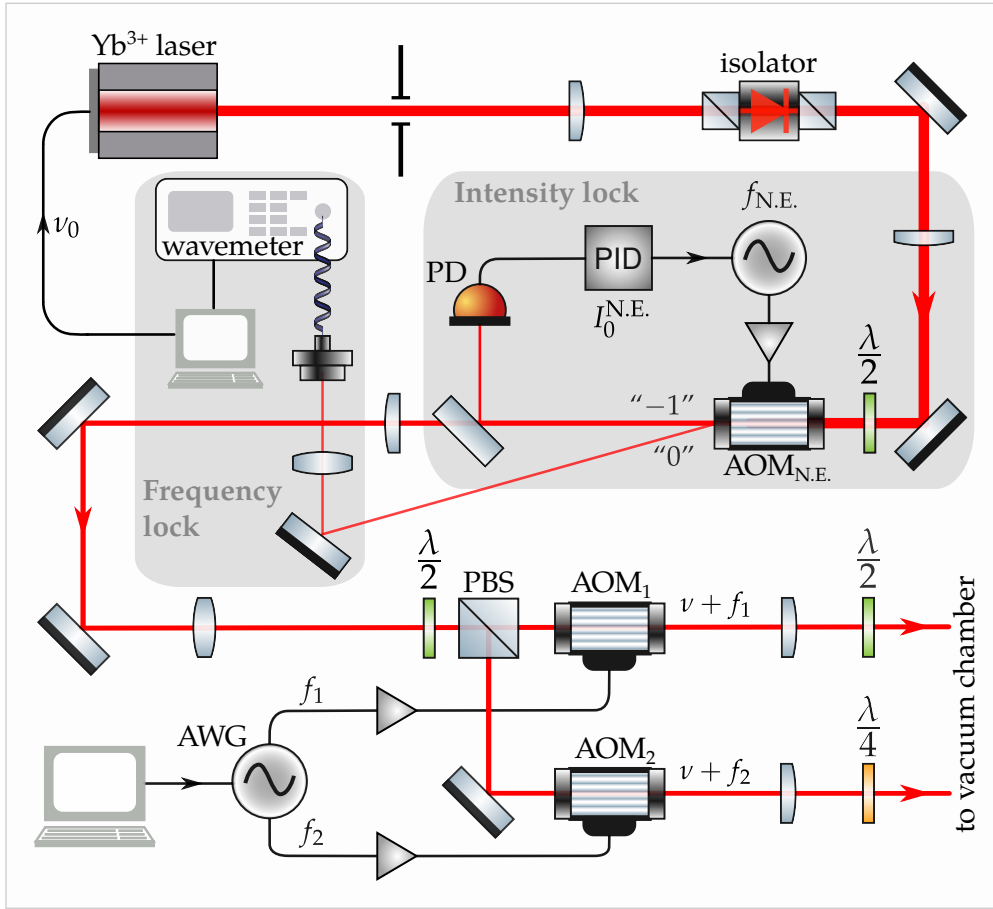
Figure 5.1: Bragg/Raman beams layout. The laser output is intensity ($I_0^{\text{N.E.}}$) and frequency (ν_0) stabilised before being split into the two Bragg (or Raman) beams at the beam splitter (PBS). Intensity lock ("noise eater", "N.E.") includes: the acoustic-optic modulator $\text{AOM}_{\text{N.E.}}$ operating in the "-1" diffraction order; the photodiode (PD) and PID-controller; the r.f. signal generator with a driving frequency $f_{\text{N.E.}}$. Pulses in each of the Bragg/Raman beams are independently controlled by the modulators AOM_1 and AOM_2. The arbitrary waveform generator (AWG) produces two pulsed phase-locked signals with the central frequencies f_1 and f_2 to drive AOM_1 and AOM_2. The resulting pair of beams with the shifted light frequencies $\nu + f_{1,2}$ drives either Bragg or Raman transition depending on the corresponding resonance condition set by the relative detuning $\Delta f = f_2 - f_1$. The final $\lambda/2$- and $\lambda/4$-wave plates control the π- and σ-ploarizations for the Raman process respectively. The beams are routed into the BEC chamber as shown in Fig. 5.2.

into the wavemeter (Burleigh WA-1100) to enable frequency locking of the laser by software means. This provides a long-term stabilisation of the frequency ν_0 in laser output to $\sim$100 MHz accuracy. Both locks enable repeatability of the experiment on long time-scales (months).

The actual Bragg/Raman beams are controlled with the modulators AOM_1 and AOM_2 (NEOS-???) with a nominal acoustic frequency $f_0^{\text{AOM}} = 80$ MHz. Both $\text{AOM}_{1,2}$ operate in the "$+1$" diffraction order with efficiency $\sim$85% (beams were focused at the AOMs crystal to the waists of $\sim$0.6 mm). The maximum attainable optical power at the output in each of the Bragg/Raman beams was 210 mW (before entering the vacuum chamber). Signals for the $\text{AOM}_{1,2}$ drivers are supplied from the phase-locked channels of the arbitrary waveform generator AWG (Keysight-33600A) with a sample rate
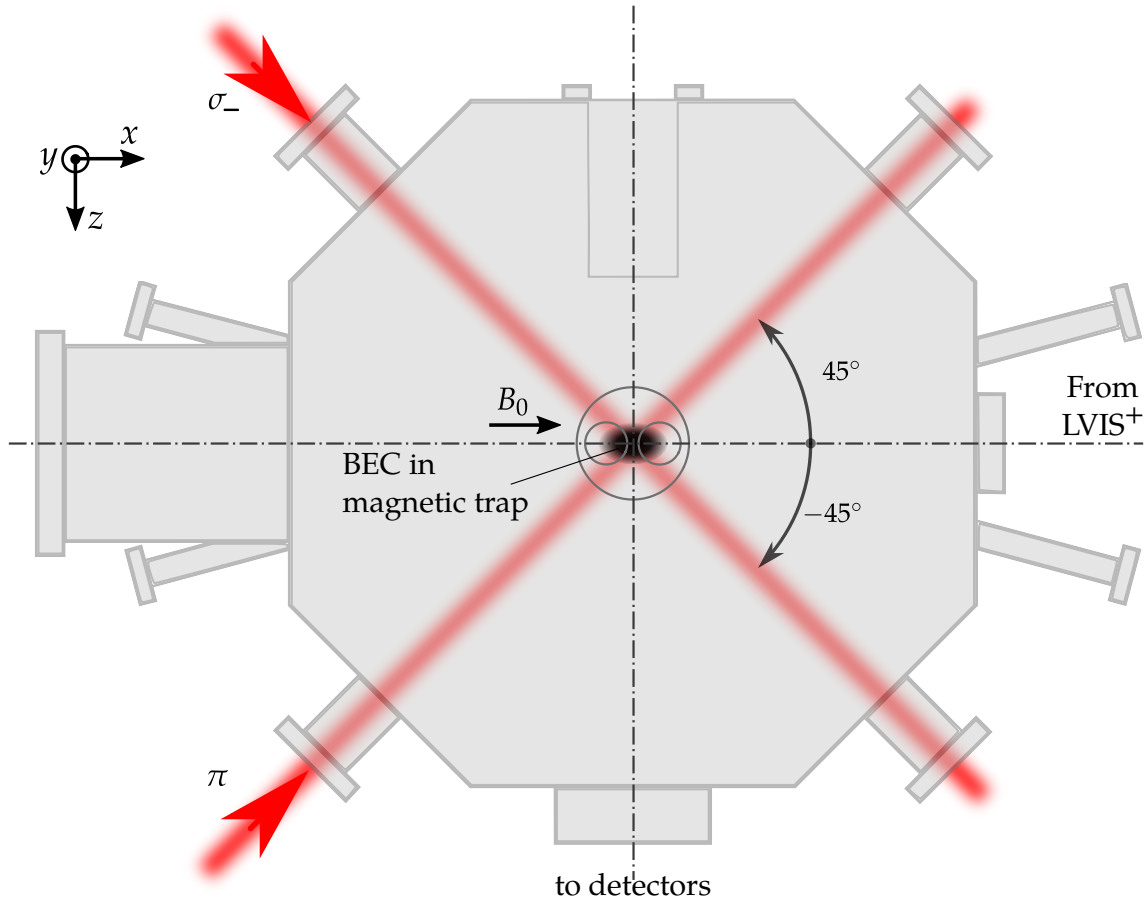
Figure 5.2: Schematic of the Bragg/Raman beams entering the vacuum chamber.
The laser beams (red) form an angle of $\theta = 90°$ and fully overlap with
trapped atoms (dark cloud, not to scale). Polarization of light (π, σ^-) is
chosen to enable Raman transition with the momentum transfer down-
wards the z-axis (see Figs. 5.4, 5.7). The π-polarization is in the xz-
plane of the chamber. Also shown a cross-section of the magnetic trap
coils (BiQUIC, not to scale) with the bias field B_0 along the x-axis.

of 1 GS/s. AWG allows for the software pre-programmed waveforms with the central
frequencies f_1 and f_2, therefore providing the relative frequency difference between the
beams $\Delta f = f_2 - f_1$ needed to stimulate a two-photon transition.

Since the intensity stabilization $\text{AOM}_{\text{N.E.}}$ operates in "-1" acoustic diffraction order,
it imposes the light frequency shift $f_{\text{N.E.}} = -120$ MHz and, therefore, the final frequen-
cies of Bragg/Raman beams are $\nu_{\text{B/R}} = (\nu_0 - f_{\text{N.E.}} + f_{1,2}) \simeq (\nu_0 - f_{\text{N.E.}} + f_0^{\text{AOM}})$. In
the following (for example, when quantifying the detuning of the laser beams from the
$^4\text{He}^*$transition resonances), we neglect the term $(-f_{\text{N.E.}} + f_{1,2}) \simeq 40$ MHz in the final
light frequency and approximate it as $\nu_{\text{B/R}} \approx \nu_0$, because it is small relative to the detun-
ing of a few GHz from the $^4\text{He}^*$resonance, – the regime we use in the experiments. (See
also the atom interferometry setup in Fig. 8.2 of chapter 8, which uses the Bragg regime
only).

The geometry of the laser beams for *s*-wave scattering experiments is shown in
Fig. 5.2. The two Bragg/Raman beams enter the BEC chamber through the 45° and

$-45°$ ports.[1] The beams stimulate either Bragg or Raman transition depending on the resonance condition set by the relative detuning Δf. The direction of the beams and the angle between them θ were chosen from considerations of *s*-wave scattering experiments. The vertical direction of the momentum transfer ensures that the atoms are fully captured as they fall onto the detector (MCP/DLD) and not hit the walls of the vacuum chamber, the angle $\theta = 90°$ leads to the size of an *s*-wave halo fitting onto the detector plates (80 mm in diameter).

We design the dual, Bragg or Raman, mode of operation, which dictates the polarization setting for each beam. The linear (π) and left-circular (σ^-) polarizations must be carefully aligned to impose the selection rules for the Raman transition to occur between the relevant magnetic sublevels. As discussed in detail below, this means absorption of a photon from the (σ^-)-mode followed by stimulated emission into the (π)-mode. We found that to achieve a nearly 99% efficiency of the Raman process, the waveplates need to be set to or better than $\sim 1°$. Since the Raman beams operate on a BEC in the magnetic trap, the π and σ^- directions are dictated by the magnetic trap bias field $\mathbf{B}_0 = (B_0, 0, 0)$ (which sets a quantisation axis). In our BiQUIC trap, $\mathbf{B}_0$, to a good approximation, points between the axes of the trap coils, i.e., aligned with the *x*-direction in Fig. 5.2. (Refer to the discussion on the effect of the magnetic field stabilization coils ("nuller") on $\mathbf{B}_0$ in appendix A.2). As seen from the symmetry of the experiment, both beams, in principle, could have either polarization, thus defining the momentum transfer direction either up or down. The choice of polarizations in Fig. 5.2 yields the downwards momentum transfer in the Raman process,– this is advantageous, for example, for the Raman atom laser experiments. Alternatively, if the atoms are upwards kicked, under gravity they will travel again through the trap position, hence there would be additional interaction with a possible leftover of BEC which is still in the trap.

5.1.2   Transitions diagram

Once the beams and their polarizations are in place, there is only one set of parameters left to affect the two-photon process – frequencies f_1 and f_2 (see Fig. 5.1), and the relative detuning between the beams $\Delta f = f_2 - f_1$. In the following we describe how, by choosing Δf corresponding to a resonance of a certain type of the process, we can drive either Raman transition or Bragg/Kapitza-Dirac diffraction, on demand, with the same pair of laser beams.

Fig. 5.3 shows the relevant Bragg and Raman transitions available in the experiment geometry and for the polarizations described above. (See also the complete levels diagram in Fig. 2.1 and the transition frequencies in table 2.1, ch. 2). The laser frequency ν_0 is blue-detuned by δ from the single-photon resonance of a ^{4}He* transition. Here we choose to operate near the $2^3S_1 \rightarrow 2^3P_0$, because the 2^3P_0 level represents only one magnetic sublevel. This greatly simplifies the Raman regime by reducing a number of possible channels for transition between the magnetic sublevels of different levels.[2] To minimise the spontaneous, single-photon scattering, we use relatively large laser detun-

---

[1]As the ports are already used for laser cooling beams in the second MOT, one of the MOT beams is reflected into the chamber off a mirror attached to a motorised flipper mount while the other flipper used for another Bragg beam. We have not observed any degradation of performance related to the use of an motorised flipper for one of the Bragg beams. Since the flipper is less mechanically stable than a static mirror, it was placed as close as possible to the re-entrant window of the chamber.

[2]For atom interferometry in the Bragg regime we operate near the $2^3S_1 \rightarrow 2^3P_2$ transition, see section 8.3.1.
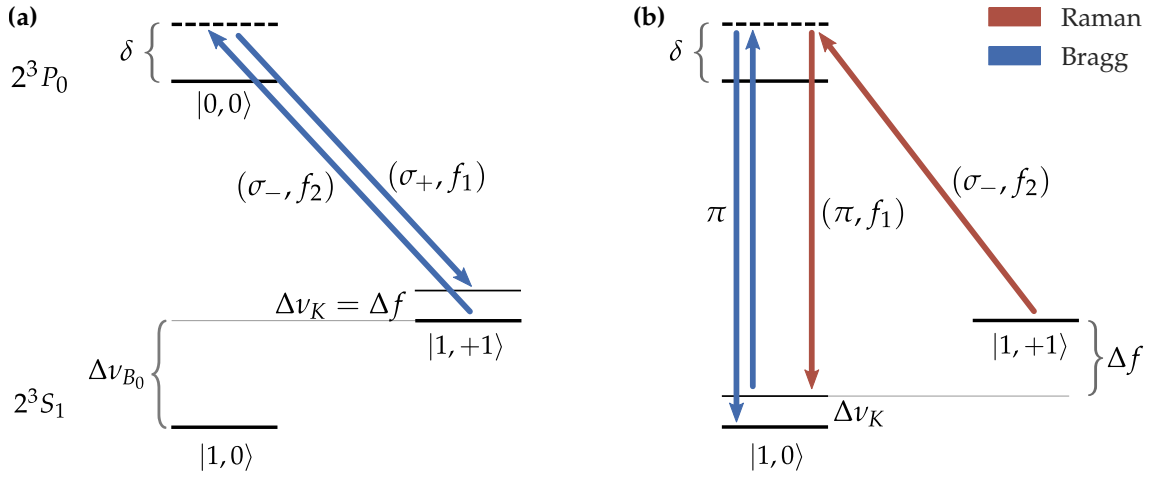
Figure 5.3: Energy level scheme for Bragg and Raman scattering. $|J, m_J\rangle$ are states of the 2^3P_0 and 2^3S_1 manifolds in ^{4}He*, (state $|1, -1\rangle$ of 2^3S_1 is not shown). The atoms in $|1, +1\rangle$ are magnetically trapped. The arrows indicate the interactions with the laser light which may be σ or π polarized. Laser detuning from the $2^3S_1 \rightarrow 2^3P_0$ single-photon transition is $\delta \gg \Delta f$, and $\Delta\nu_{B_0}$ is a Zeeman splitting of the m_J-sublevels, $\Delta\nu_K$ is the separation between (external) momentum states. The atom acquires the kinetic energy $\Delta E_K = h\Delta\nu_K$ and changes its momentum state after the Bragg or Raman transition. **(a)**, Bragg transition is stimulated by the laser beams with polarizations σ^- and σ^+ and the relative detuning $\Delta f = f_2 - f_1$; **(b)**, Raman transition (red arrows) followed by the Bragg (blue arrows).

ings of the order of $\delta = 2 \dots 10$ GHz. We detune to the blue as to avoid the two-photon scattering also to happen via the 2^3P_2 manifold of 5 magnetic sublevels. In the diagram, as well as in the following expressions, we use the indices "1" and "2" (e.g. in f_1 and f_2) for the parameters of the beam a photon is emitted to and absorbed from respectively.

Starting with a trapped BEC in the $|1, +1\rangle$ state we can drive either Bragg (Fig. 5.3(a)) or Raman (Fig. 5.3(b)) transition, or a sequence of transitions: Raman, immedeately followed with Bragg (Fig. 5.3(b)). The restrictions on light polarization imposed by selection rules (see section 2.4 for details) mean that the Bragg pulses will underutilize the laser power in the beams, since only a half of the power is of the correct polarization: $(\sigma^- + \sigma^+)/\sqrt{2} = \pi$. For example, the Bragg transition in Fig. 5.3(a) requires a right-circular polarization σ^+, but the avaliable beam is π-polarized. Generally, as it is possible to supply a σ-polarization with a π-polarised beam and vice versa, – we can drive both Raman and Bragg transitions with the same pair of beams, without the need to realign polarizations. It is also possible to apply the Raman and then Bragg transitions in succession, this is demonstrated in Fig. 5.3(b): Raman outcoupling into the untrapped state ($m_J = 0$) with a non-zero momentum, which is then brought into a zero-momentum state by the Bragg transition. As a net result of this sequence, the atoms have been transferred between the internal states only: $|1, +1\rangle \rightarrow |1, 0\rangle$, without a change in momentum.

The requisite that enables the transition in the Bragg or Raman regime is the relative detuning Δf, which is given by the conservations of total energy and momenta. After a two-photon transition, the change in the kinetic energy of an atom is

$$\Delta E_K \equiv h\Delta\nu_K = \Delta p_{\text{He}}^2/2M_{\text{He}}, \tag{5.1}$$

where $\Delta\nu_K$ is the separation energy between momentum states in frequency units and

$(\alpha_1, \alpha_2) = (45.0°, -45.0°)$
$\Delta\nu_K = 84.95$ kHz
$|\Delta\mathbf{p}^{\text{He}}|/\hbar k_0 = 1.41$
$\Delta p_x^{\text{He}}/\hbar k_0 = 0.00$
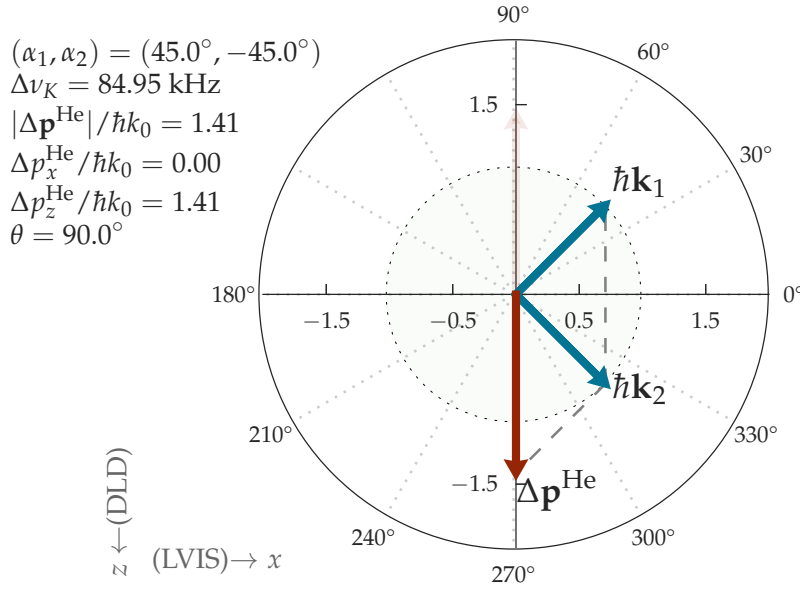$\Delta p_z^{\text{He}}/\hbar k_0 = 1.41$
$\theta = 90.0°$

Figure 5.4: Momenta diagram for the Bragg/Raman process. The laser beams at the angles of 45° and −45° as for the experimental configuration in Fig. 5.2. The stimulated transition occurs by absorption of $\hbar\mathbf{k}_2$-photon and emitting $\hbar\mathbf{k}_1$-photon. In the case of Bragg transition (from a zero-momentum state) only, the direction of the process is set by the sign of the detuning $\Delta f = \pm\Delta\nu_K$, which results in the two possible momentum directions: $\pm\Delta\mathbf{p}^{\text{He}}$. The relevant quantities in Eqs. (5.2) and (5.3) are shown on the left.

M_{He} is the mass of an atom. The corresponding change of the atomic momentum is (Fig. 5.4):

$$\Delta p_{\text{He}} = |\hbar\mathbf{k}_2 - \hbar\mathbf{k}_1| = 2\hbar k_0 \sin\frac{\theta}{2}, \tag{5.2}$$

where $|\hbar\mathbf{k}_1| \cong |\hbar\mathbf{k}_2| = \hbar k_0$ is a single photon momentum and θ is the angle between the beams. This yields

$$\Delta\nu_K = \frac{2h\nu_0^2}{M_{\text{He}}c^2} \sin^2\frac{\theta}{2}, \tag{5.3}$$

where $\nu_0 = c/\lambda$ is a laser frequency ($\lambda \cong 1083$ nm). For the Bragg process, since the internal state does not change, the photon detuning Δf is simply a separation of the momentum states: $|\Delta f| \equiv \Delta\nu_K$ and $h\Delta\nu_K$ is the energy difference between two photons from each of the Bragg beams. For the Raman scattering, however, the change of the internal state alters the total energy of an atom in magnetic field due to the Zeeman splitting ($\Delta\nu_{B_0}$) between sublevels of the 2^3S_1 manifold (Fig. 5.3). Therefore, the total energy difference between the initially trapped ($m_J = +1$) state and the final state $m_J = 0$ with a non-zero momentum after transition is $|\Delta\nu_{B_0} - \Delta\nu_K|$. In the magnetic trap with a bias field magnitude B_0 (in Gauss), the splitting between 2^3S_1 sublevels is given by

$$\Delta\nu_{B_0}[\text{MHz}] = B_0\frac{\gamma_e}{2\pi} = B_0[\text{G}] \times 2.8025[\text{MHz/G}], \tag{5.4}$$

where γ_e is the gyromagnetic ratio of an electron, which determines a magnetic moment for $^4\text{He}^*$.

Analogously to the two-photon, or first order, Bragg process, we can excite second and higher order Bragg multi-photon transitions by satisfying energy conservation in

Eq. (5.1) via replacing $\Delta\nu$ with $\ell^2\Delta\nu$ and Δp_{He} with $\ell\Delta p_{\mathrm{He}}$, where integer ℓ is the diffraction order. Furthermore, we can enter the Kapitza-Dirac regime if the spectrum of the Bragg pulses is broad enough to excite several higher order transitions simultaneously, i.e. multiple conditions on relative detuning are satisfied within a single pulse: $\Delta f_\ell = \pm\ell^2\Delta\nu_K$, $\ell = 1\ldots L$, where L is the highest diffraction order.

Summarising, the relative frequency detunings between the laser pulses which enable a resonance for a certain transition type are:

$$
\begin{aligned}
\text{Bragg:} &\quad \Delta f = f_2 - f_1 = \pm\Delta\nu_K, \\
\text{Raman:} &\quad \Delta f = f_\sigma - f_\pi = -(\Delta\nu_{B_0} - \Delta\nu_K), \\
\text{Multi-photon } \ell\text{-th order Bragg:} &\quad \Delta f = \pm\Delta\nu_K\ell^2, \\
\text{Kapitza-Dirac :} &\quad \Delta f \text{ is a continuous spectrum,}
\end{aligned}
\tag{5.5}
$$

where different signs of $\Delta\nu_K$ in the Bragg process correspond to the two opposite momentum transfer directions (Fig. 5.4), and $f_\sigma - f_\pi \equiv f_2 - f_1$ is the detuning between π and σ^- polarized beams in the Raman process. Since the process is polarization selective, the direction of momentum transfer is predefined by the fixed configuration of laser beams. The level diagram also shows that, to enable the Raman process via the 2^3P_0 level[3] it is necessarily $f_\sigma < f_\pi$.

Note that the diagram in Fig. 5.3 is not to scale, that is, the relation between the quantities is $\Delta\nu_K < \Delta\nu_{B_0} \ll \delta \ll \nu_0$. For our experimental parameters, the Zeeman splitting is typically $\Delta\nu_{B_0} = 0.7\ldots 12$ MHz, depending on desired trapping frequencies and the "nuller" setting. On the other hand, the splitting between the momentum states $\Delta\nu_K$ is on the order of tens of kHz, set by the angle between the laser beams, varying from 3 kHz to a maximum of 170 kHz for the angles $\theta = 15°$ or $180°$ respectively (Eq. (5.3)). See also appendix A.3 for parameters of the other Bragg geometries accessible in our experiment.

5.1.3 Waveforms of the laser pulses

As discussed in the previous sections, spectral content of the pulsed waveforms, as well as the relative detuning between them, – are sufficient for a full control of a particular two-photon process. This is convenient, as the waveforms can be preprogrammed, stored, and then uploaded to the generator at the runtime of experiments. The rf waveforms driving the Bragg/Ramn AOMs for each of beams are defined as:

$$
\begin{aligned}
u_1(t) &= A\,w(t)\sin(2\pi f_1 t), \\
u_2(t) &= A\,w(t)\sin(2\pi f_2 t),
\end{aligned}
\tag{5.6}
$$

where A is an amplitude and $w(t)$ is a slowly varying pulse envelope. The carrier frequencies of $u_1(t)$ and $u_2(t)$ are set to:

$$
\begin{aligned}
f_1 &= f_0^{\mathrm{AOM}} - \Delta f/2, \\
f_2 &= f_0^{\mathrm{AOM}} + \Delta f/2,
\end{aligned}
\tag{5.7}
$$

such, that depending on the type of transition we want to drive – Bragg or Raman, Δf is defined in Eq. (5.5). For best efficiency, the frequencies $f_{1,2}$ defined as above have

---

[3]In the case of the Raman transition via the 2^3P_2 level, the sign reversal of Δf would also reverse the momentum transfer, similarly to how it occurs in the Bragg regime.
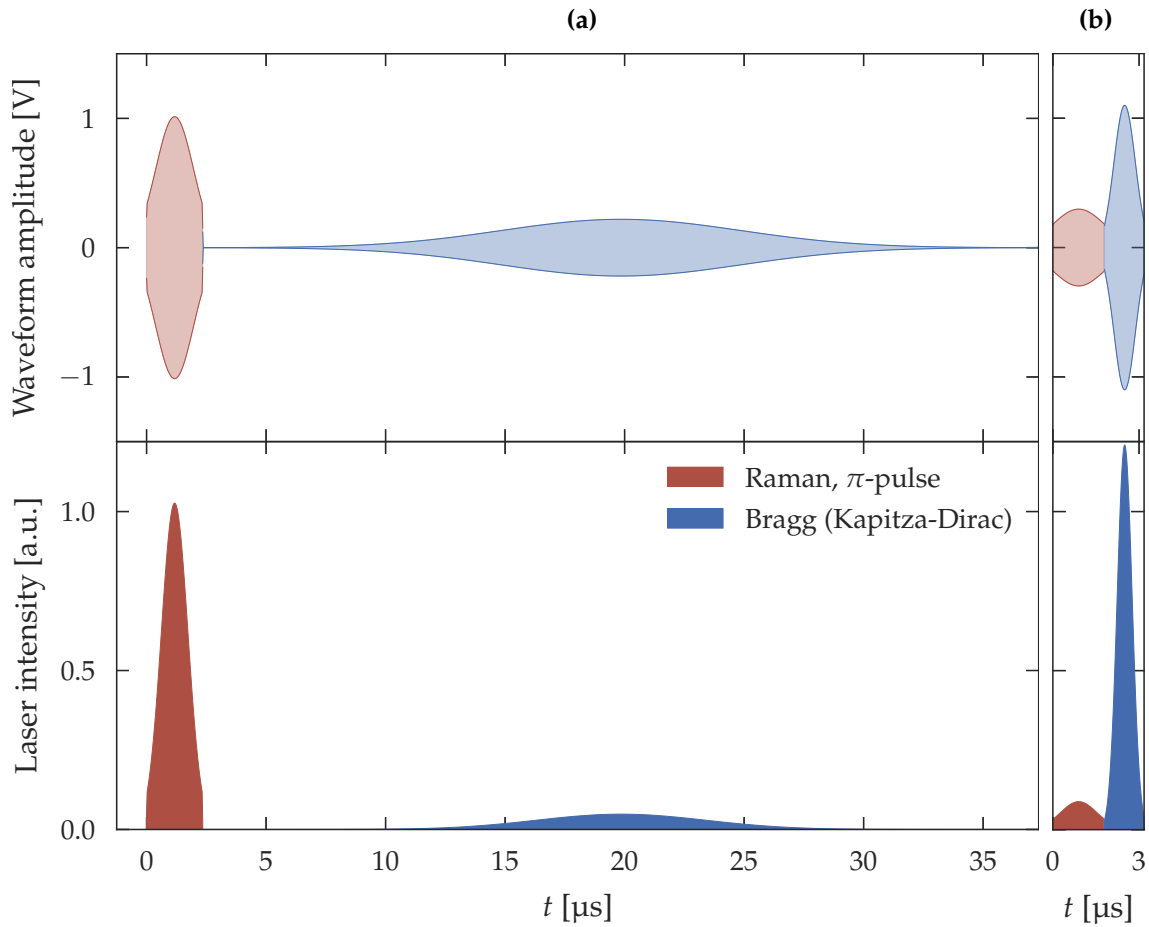
Figure 5.5: Pulse temporal envelope of the Raman/Bragg sequence. Analog waveform $u_{1,2}(t)$ (top) from Eq. (5.6) and the resulting pulse intensity (bottom) used to drive acousto-optic modulators for **(a)** Raman/Bragg, and **(b)** Raman/Kapitza-Dirac pulse sequences.[#TODO: ADD FFT + SHOW SPACING FOR BRAGG LEVELS/ORDERS.]

minimal deviation from the nominal frequency of the AOM $f_0^{\text{AOM}} = 80$ MHz. Decrease in the AOM diffraction efficiency is particularly noticeable for the Raman pulses, where Δf can be up to $\sim$10 MHz.

Both Raman and Bragg pulses are modulated (apodized[4]) to control the power spectral density of the pulses via Fourier broadening. The modulation window function is applied to the waveform data prepared for the AWG as an array of voltages. As a modulation envelope we use the Gaussian window function (discrete apodization function):

$$w[n] = \exp(-n^2/2\sigma^2) = \exp\left[-\frac{1}{2}\left(\alpha\frac{n}{(N-1)/2}\right)^2\right], \qquad (5.8)$$

where $n \in [-(N-1)/2, (N-1)/2]$ are indices of the waveform data array.

add FFT spectrum

Several pulsed waveforms, each for a particular type of the transition, form a pulse sequence.

---

[4]Apodization is a technique of transforming the signal profile to smooth the discontinuities at the beginning and the end of a sampled waveform.
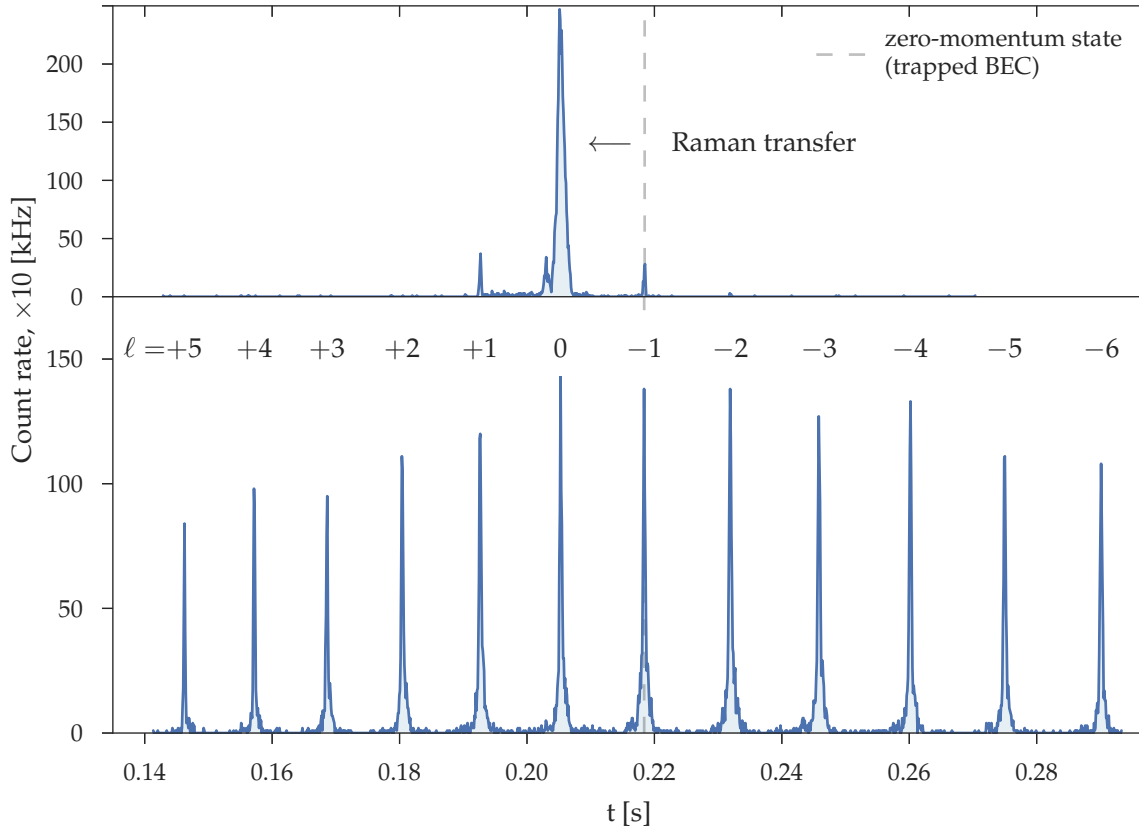
Figure 5.6: Kapitza-Dirac effect: time-of-flight data. A single experimental run without (top) and with (bottom) the diffracting pulse after Raman outcoupling into $m_J = 0$ state. Indices mark the diffraction orders $\ell = +5 \ldots -6$, where $\ell > 0$ for momentum transfer in the positive z-direction (downwards). The momentum state $\ell = +5$ arrives onto the detector first.

5.1.4 Raman and Bragg scattering of BEC

Fig. 5.5 shows the actual waveforms used for *s*-wave generation.

Raman/Bragg sequence

Raman π-pulse duration is $t_R^{(\pi)} = 2.35$ μs, Bragg $\pi/2$-pulse duration is $t_B^{(\pi/2)} = 35$ μs, amplitude peaks are $K_R = 0.96$ and $K_B = 0.208$ respectively, modulation factors $\alpha_R = 1.5$ and $\alpha_B = 3.5$; $E_K = 84.9$ kHz;

$\Delta\nu_{B_0} = 3.618$ MHz.

In the experiment, $\Delta\nu_{B_0}$ is measured by finding the trap bottom with accuracy on the order of a chemical potential of a BEC ($\sim 5 \ldots 10$ kHz). This provides a starting value for Δf, which is then fine-tuned with 1 kHz accuracy using actual Raman π-pulse, – this accounts for other factors, such as AC Stark shift.

[#TODO: MAKE A TABLE of PARAMETERS]

Note, that to reverse the momentum transfer direction in the Bragg process it is sufficient to change the sign of Δf

Raman/Kapitza-Dirac sequence

$t_R^{(\pi)} = 1.8$ μs, $t_B = 1.4$ μs, $K_R = 0.270$ and $K_B = 1.0$ $\alpha_R = 1.0$ and $\alpha_B = 1.9$;

5.2   *s*-wave scattering experiments

To produce an *s*-wave halo, we collide atoms in the BEC in two steps: (i) first we outcouple nearly all atoms from the trap via a two-photon Raman transition to the magnetically insensitive sublevel $m_J = 0$, and then (ii) diffract the cloud into multiple momentum modes. This last step introduces a relative momentum difference between atoms in the different diffraction orders, which then generate a series of *s*-wave scattering halos via binary collisions between atoms in different orders. We employ the same laser beams for both Raman and Kapitza-Dirac pulses, with the latter Fourier-broadened to ensure we are in the Kapitza-Dirac regime, which populates multiple diffraction orders.

Figure 5.7: Schematic of the *s*-wave scattering experiment. The experiment starts by using Bragg or Kapitza-Dirac diffraction laser beams along $(\mathbf{e}_x \pm \mathbf{e}_z)/\sqrt{2}$ (yellow arrows, as in Fig. 5.2) to split the BEC cloud outcoupled from the trap ($m_J = 0$) into different momentum states along $\mathbf{e}_z$ (for simplicity, only the 1st diffraction order is shown as the clouds evolve in time). Binary atomic collisions populate an *s*-wave scattering halo with correlated pairs of nearly opposite momenta ($\pm\mathbf{k}$), which then expand as atoms free-fall under gravity ($\mathbf{g}$) onto the detector (MCP/DLD). In the momentum space associated with the center-of-mass reference frame the BECs are situated at opposite poles of the *s*-wave scattering sphere.
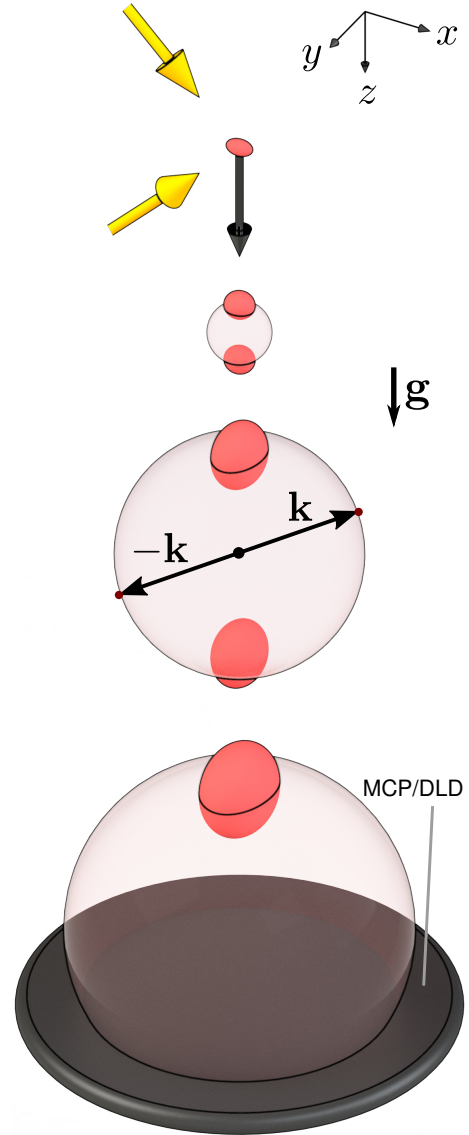
Both Raman and Kapitza-Dirac pulses propagate along the $(\mathbf{e}_x \pm \mathbf{e}_z)/\sqrt{2}$ directions, where $\mathbf{e}_{x,y,z}$ is the unit vector along the x, y, z direction, as shown in Fig. 5.7. The direction of the beams and angle between them θ were chosen from the considerations of *s*-wave scattering experiments. This results in momentum transfer along the vertical z axis, with the momentum difference between any two adjacent diffracted orders (from Eq. (5.2)):

$$\hbar\Delta\mathbf{k} = \pm\sqrt{2}\hbar k_0\mathbf{e}_z, \tag{5.9}$$

where $\hbar k_0$ is a single photon recoil, $k_0 = 2\pi/\lambda$, and $\lambda = 1083.1979$ nm is the photon wavelength. In k-space associated with the center-of-mass reference frame, each *s*-wave scattering halo comprises atoms on a sphere of radius

$$k_r = |\Delta\mathbf{k}|/2 = k_0/\sqrt{2}, \tag{5.10}$$

which reflects energy and momentum conservation, as shown in Fig. 5.7.

Kapitza-Dirac diffraction produces 12 diffraction orders $-6\ldots+5$ along $\mathbf{e}_z$. Collisions between each pair of adjacent orders result in 11 independent scattering halos.

After the collision, the expanding halo falls $\sim$850 mm under gravity onto a multi-channel plate and delay-line detector, which records the arrival positions and time (x, y, t) of individual atoms. We then transform this 3D information into the momenta (k_x, k_y, k_z) of individual atoms, which is plotted in Fig. 5.8 to show the eleven halos produced in the collision process.

We employ the same laser beams for both Raman and Kapitza-Dirac pulses, only changing the relative frequency detuning of the waveforms, which is set by the bias B_0 and geometrical angle between the beams (90°). The laser is blue detuned by 2 GHz from the 2^3S_1–2^3P_0 transition. The Raman transition in the beginning of the sequence also results in the cloud acquiring a momentum change of $\sqrt{2}\hbar k_0\mathbf{e}_z$, which sets the center-of-mass of the cloud in downward motion. The duration of the outcoupling Raman π-pulse is $t_\pi = 1.8$ μs, with $\sim$95% transfer efficiency. It is then immediately followed by a 1.4 μs Kapitza-Dirac pulse. The maximum intensity of each laser beam is $\sim$450 mW/mm^2 for the Raman pulse and $\sim$30 mW/mm^2 for the Kapitza-Dirac pulse. Each of the pulse sequences is modulated with an overall Gaussian envelope to control Fourier-broadening. Thus, the broadening of the Raman pulse was optimised to maximise the transfer to the magnetically insensitive sublevel $m_J = 0$, while the Kapitza-Dirac pulse was set to maximise the number of diffraction orders generated (L).

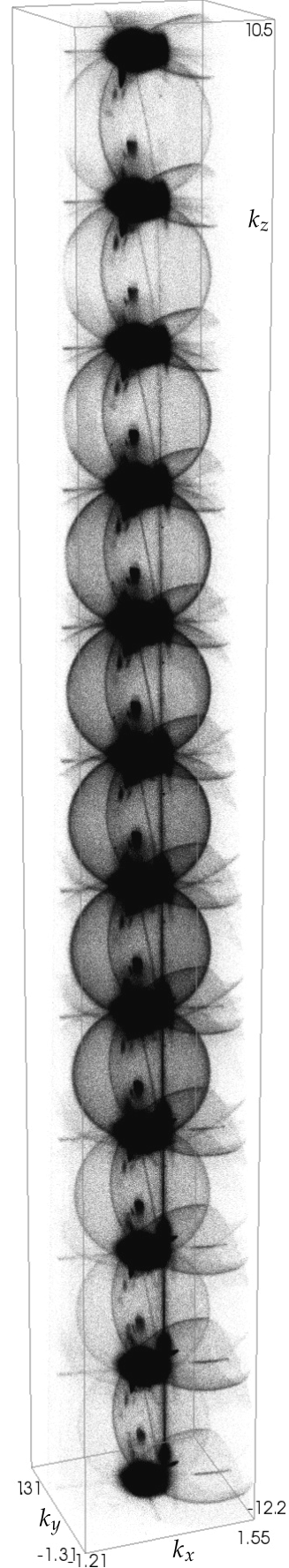In our experiment we have achieved $L = 12$ orders, con-

Figure 5.8: KD effect.

sequently producing $L - 1 = 11$ *s*-wave halos between the adjacent orders, as pictured in Fig. **??**b. In principle, by increasing the laser power of the diffraction beams, one could raise L even further, generating more halos with lower density and therefore possessing higher correlations. It is, however, optimal to have $L = 12$ for the ghost imaging configuration in our experiment because of the relatively high absolute velocity of the ^{4}He* atoms in the higher diffraction orders, i.e. for $\ell = \pm 6$ it is $v_z = \pm 78$ cm/s. There are two problems which arise for $|\ell| > 6$ in our setup: (i) fast travelling, downwards-kicked halos do not expand enough to cover the object mask before falling onto the detector (Fig. **??**c), and (ii) upwards-kicked halos will be lost through hitting the top of the vacuum chamber.

It is also interesting to note that we observe larger-diameter halos from the non-adjacent orders $(\ell, \ell + 2)$, which are reconstructed only partially since they expand beyond the detector size. In principle, $g^{(2)}$ peaks should be higher for these larger halos, since the scattering modes overlap less [36]. However, the population of these halos is too low to make them usable here.

Note that the non-zero halo thickness δk (rms) of the halo is due to uncertainty-limited broadening from the finite size of the condensates, as well as mean-field interactions in the BEC during expansion of the halo. In our experiments we observe $\delta k / k_r = 0.034(\pm 0.003)$.

The dark clouds represent BEC's in different diffraction orders ℓ with an *s*-wave halo situated between each of the corresponding orders $(\ell, \ell + 1)$. The center of each halo is on the momentum transfer axis z. Also clearly visible are the portions of larger-diameter halos from non-adjacent orders $(\ell, \ell + 2)$, etc., as well as halos formed by single-photon spontaneous scattering from the diffraction laser. The halo populations follow that of different orders in the Kapitza-Dirac effect, and as a consequence, the average number of atoms per halo decreases from ~ 370 for $(\ell, \ell + 1) = (0, +1)$ to ~ 50 for $(+5, +6)$.

Fig. 5.8 shows a 3D view in *k*-space. It utilises data from 10,000 experimental runs with total of $\sim 9 \times 10^7$ counts.

Fig. 5.6 shows time-of-flight[5] data for the Kapitza-Dirac sequence. Remaining atoms in magnetic trap are dropped ~ 0.5 s after. Diffraction orders which acquire downward momentum arrive first onto the detector, and therefore, spend less time being accelerated by gravity; this makes the time separation between the orders $\ell = +5, +4$ smaller than for $\ell = -5, -6$. Sign convention is that $\ell > 0$ if the momentum transfer is in the positive *z*-direction (downwards). The order $\ell = 0$ corresponds to the momentum state of the BEC cloud immediately after Raman π-pulse and *before* the Kapitza-Dirac diffraction. Thus, here the zero-momentum state coinciding with the trapped BEC initially at rest, is $\ell = -1$ as shown in Fig. 5.6 with a dashed line.

5.3 Data analysis.

5.3.1 *k*-space representation.

From equation of motion for the single particle $\mathbf{r}(t) = \mathbf{r}(0) + \mathbf{v}(0)t + \mathbf{g}t^2/2$, expressing the initial atomic velocity $\mathbf{v}(0) = (v_x, v_y, v_z)$ transformation of the coordinates $(x, y, t) \to$

---

[5]see sec. 3.2.1 for details on time-of-flight measurements.
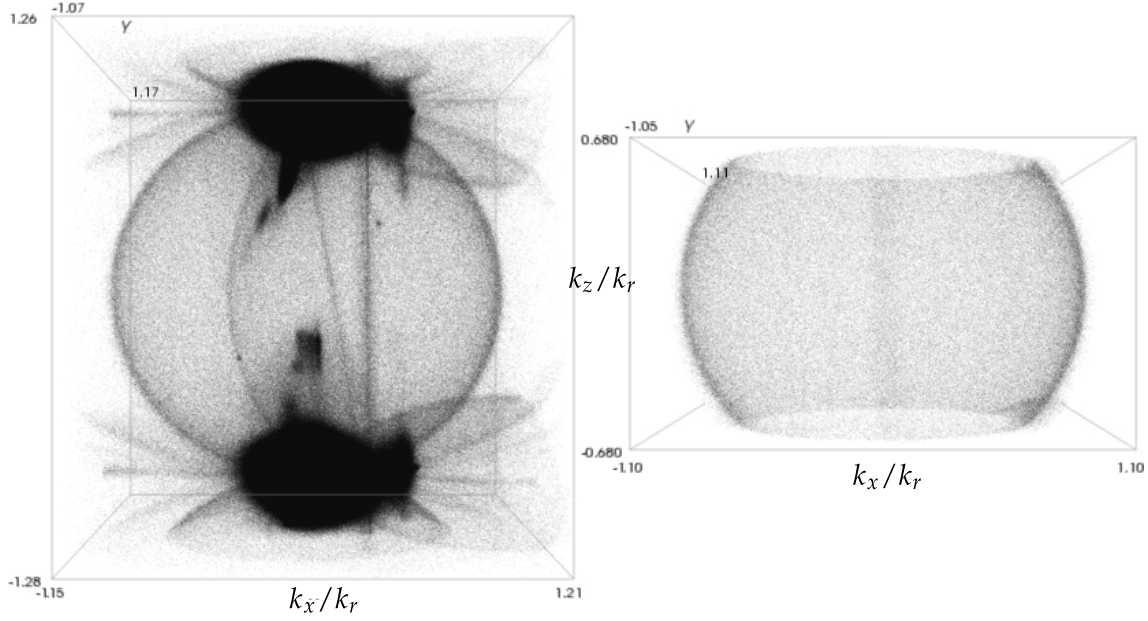
Figure 5.9: The halo data. One of *s*-wave halos formed in Kapitza-Dirac regime. Raw data in *k*-space before (on the left) and after the filtering during post-processing. The plotted data is combined of a total of 10,000 experimental runs.

(v_x, v_y, v_z):

$$v_x = (x - x_0)/t,$$
$$v_y = (y - y_0)/t, \qquad (5.11)$$
$$v_z = -z_0/t - gt/2,$$

where $g = 9.796\,\text{m/s}^2$ [43] is the acceleration due to gravity, $\mathbf{r}(0) = (x_0, y_0, z_0)$ is the initial position of the BEC, z_0 is effectively a distance between MCP/DLD and the magnetically trapped BEC, from measuring the free-fall time of $m_J = 0$ atoms: $T_f = 418.1$ ms, which yields $|z_0| = 856.2$ mm (note that $z_0 < 0$ for the coordinate system centred at the detector origin (Fig. 5.7). It is convenient to use the normalized coordinates $(k_x, k_y, k_z)/k_r$, thus always working with the unit sphere.

In addition to the *s*-wave shells of interest, the raw data also contains the counts which are not originated from *s*-wave scattering,– most notable being the diffracted BEC clouds, but also the portions of the higher order halos, as well as the stray atoms from a thermal fraction of BEC. To minimise the effect of non-halo counts, the post-processing of the data selects a region in *k*-space corresponding to an *s*-wave halo and thus, filtering out other counts. The filtering of the halo data involves: (a) cropping off the BEC clouds along $\mathbf{e}_z$ by choosing a cut-off level $\varkappa_z$ such, that only the counts with $|k_z|/k_r \leq \varkappa_z$ are kept; (b) selecting a thin spherical shell which encompasses counts from the halo, i.e. with $(1 - \varkappa_r') < k/k_r < (1 + \varkappa_r'')$, where $k = \sqrt{k_x^2 + k_y^2 + k_z^2}$. For the results presented in this and the following chapters, the cut-off levels were optimised to be $\varkappa_z = 0.68$ and $\{\varkappa_r', \varkappa_r''\} = \{0.05, 0.11\}$. As an example of the halo filtering procedure, Fig. 5.9 shows a portion of the multi-halo set from Fig. 5.8 for the halo from by the diffraction orders $(\ell, \ell+1) = (-2, -1)$. Another advantage of the chosen beams geometry is that the BECs and the main portions of the halo are separated in time as they hit the MCP/DLD, and thus do not saturate the detector.

5.3.2 Halo properties.

add TOF
+DLD-2D
plots of the
halos

Number of counts in halo.

Here the total number of counts in a halo means the counts in a complete spherical shell. We calculate it as $N = N_\varkappa/\varkappa_r$ from the known number of counts $N_\varkappa$ in the fraction of a spherical shell $k_z/k_r \leq \varkappa_r$. Accounting for a quantum efficiency $\eta \approx 10\%$ then gives the number of atoms $N_a = {N_\varkappa/\varkappa_r\eta}$ plotted in Fig. 5.10. The average number of atoms goes from $\langle N_a \rangle = 372(\pm 109)$ for the halo $(\ell, \ell+1) = (-1, 0)$ to $\langle N_a \rangle = 34(\pm 22)$ for $(+4, +5)$. As halos expand during their travel to the detector, the upwards-kicked halos slightly clip on the side windows of the BEC chamber, hence a small fraction ($< 5\%$) of these halos is lost (Fig. 5.8).
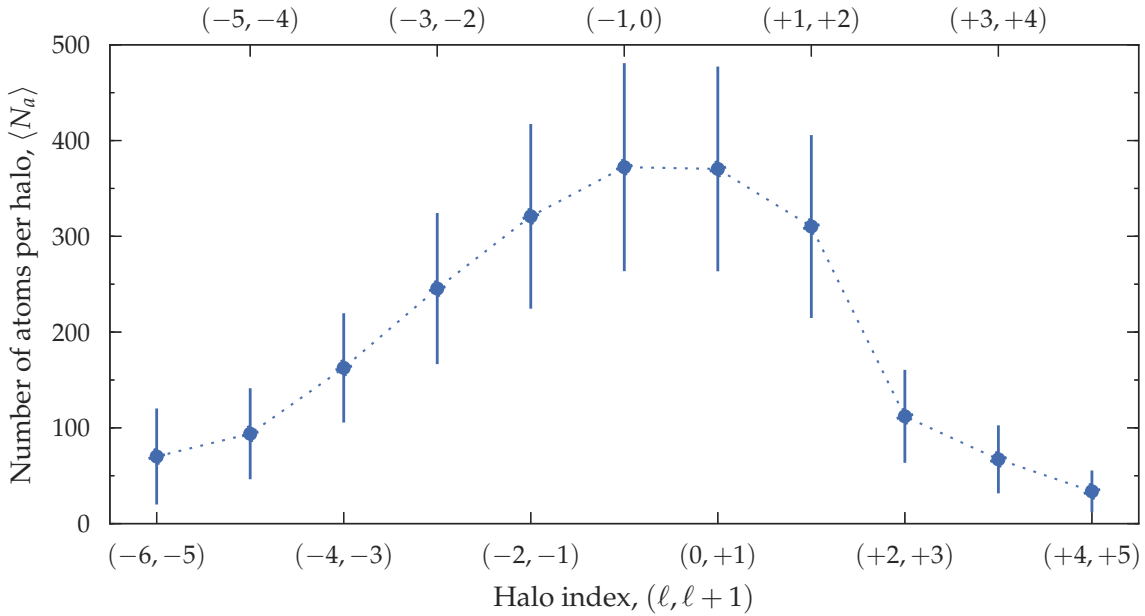

Figure 5.10: Halos populations. Average number of atoms per halo from the diffraction orders $(\ell, \ell+1)$. 2σ-error bars show the standard deviation over 54,473 experimental runs.

Particles density.

5.4 Relative number squeezing.

Following [44**?**] we characterise the *s*-wave halo production by measuring the normalised relative number variance between two different sectors of the halo containing N_i and N_j counts:

$$V_{i,j} = \frac{\text{Var}(N_i - N_j)}{\langle N_i \rangle + \langle N_j \rangle} = \frac{\langle (N_i - N_j)^2 \rangle - \langle N_i - N_j \rangle^2}{\langle N_i + N_j \rangle}, \tag{5.12}$$

where the averaging $\langle \ldots \rangle$ is taken over M experimental runs, $(N_i - N_j)$ is the relative number difference between sectors i and j. $V < 1$ in the diametrically opposite parts
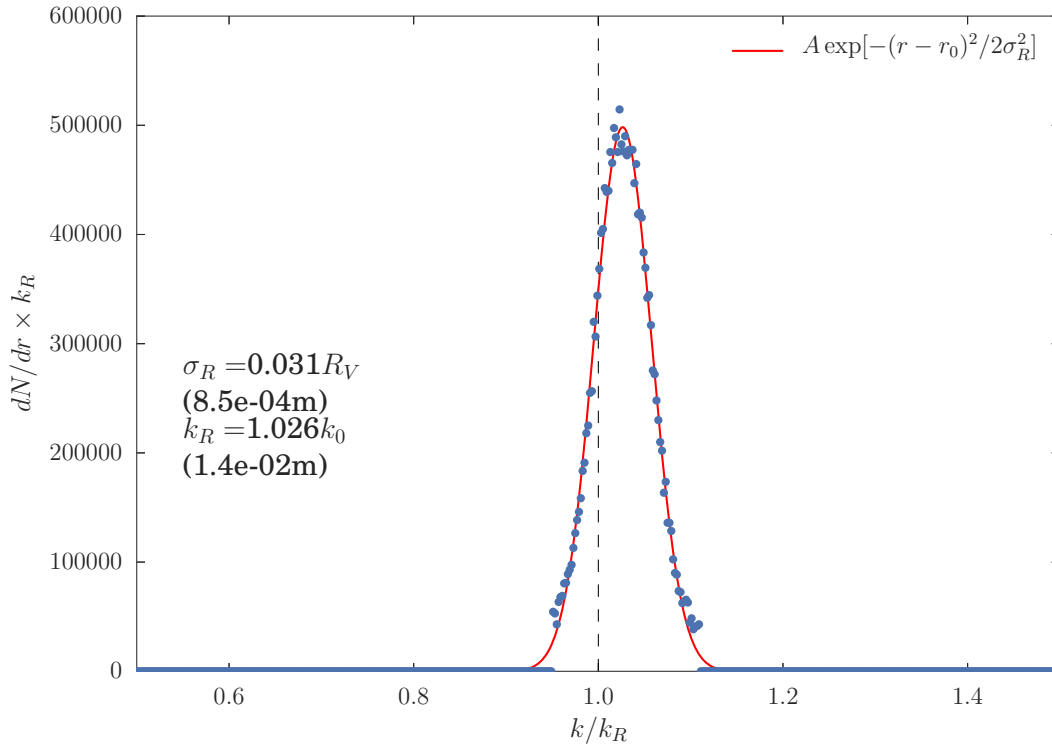
Figure 5.11: radial density.

suggests the presence of the correlated atom pairs. Using expression for the variance of the sample variance [**?**]:

$$\mathrm{Var}(\mathrm{Var}(X)) = \left[\mu_4(X)(M-1)^2 - \mu_2(X)^2(M-1)(M-3)\right] \Big/ M^3 \approx \frac{1}{M}\left(\mu_4 - \mu_2^2\right),$$

we estimate the error of the numerical evaluation of $V_{i,j}$ as:

$$\delta V_{i,j} = \frac{1}{M}\frac{\left(\mu_4 - \mu_2^2\right)}{\langle N_i + N_j\rangle}, \tag{5.13}$$

where $\mu_k(X) = \frac{1}{M}\sum_{m=1}^{M}\left(X_m - \overline{X}\right)^k$ is the k-th central moment, and $X = N_i - N_j$.
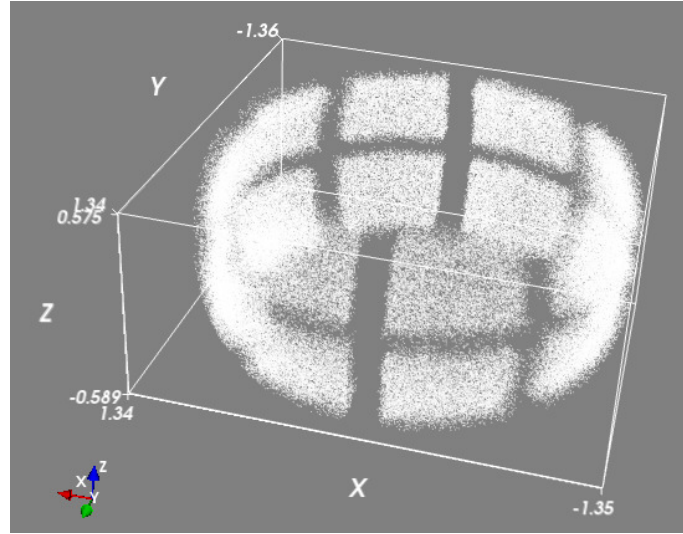
5.4.1 Detection efficiency considerations.

5.5 Kapitza-Dirac effect.

[1], p.1134

here we neglect the effects of the BEC's refractive index and mean field effects [45] on the recoil momenta $\ell\hbar k$

(a)
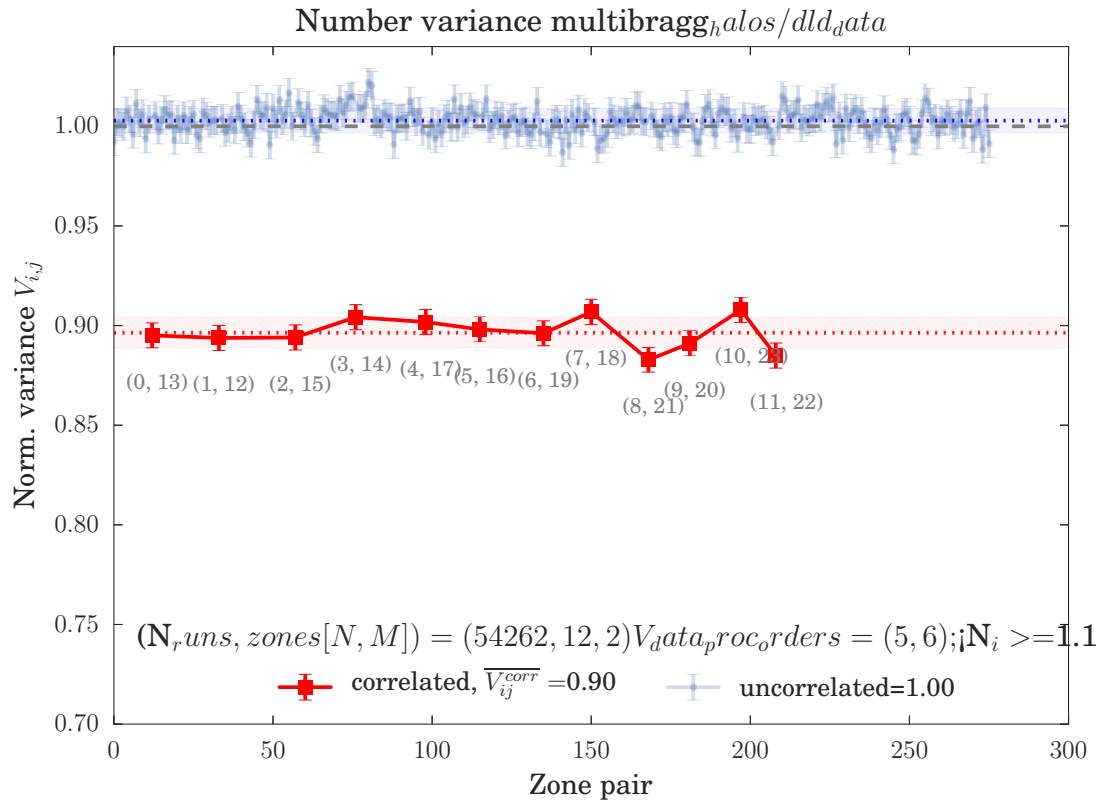

(b)

Figure 5.12: Relative number squeezing. Division of the *s*-wave halo into sectors **(a)** and the normalized relative number variances **(b)** between different sectors. Sub-poissonian variances are observed for the opposite ("correlated") sectors.

5.5.1 Multi-halos.

"artifacts+other nonliner(?) stuff"

Compensating magnetic trap oscillations.

5.6 Second order correlation function $g^{(2)}$.

For independent *s*-wave halos originating from different diffraction orders (Fig. **??**b) we construct a second-order normalised cross-correlation function in *k*-space:

$$\tilde{g}^{(2)}(\Delta \mathbf{k}) = \frac{\int d^3\mathbf{k}\, G^{(2)}(\mathbf{k}, -\mathbf{k} + \Delta \mathbf{k})}{\int d^3\mathbf{k}\, \langle n(\mathbf{k}) \rangle \langle n(-\mathbf{k} + \Delta \mathbf{k}) \rangle}, \tag{5.14}$$

where $G^{(2)}(\mathbf{k}, -\mathbf{k} + \Delta \mathbf{k})$ is the un-normalised 2 particle cross-correlation function. Because of the spherical symmetry of the *s*-wave halo in momentum space, it is convenient to perform the analysis with atomic momenta. However, to allow a spatial resolution to be extracted, the final results are converted to spatial units as $g^{(2)}(\Delta \mathbf{r})$. Since we know the time-of-flight to the detector T_f, we can change the coordinate representations of the detected atom position, from velocity (momentum) space to position space or position and time: (v_x, v_y, v_z) or $(k_x, k_y, k_z) \rightarrow (x, y, z) \rightarrow (x, y, t)$. For the spatial coordinate representation for $g^{(2)}(\Delta \mathbf{r})$ in Fig. 5.13, we convert atom velocities $\Delta \mathbf{v} = \hbar \Delta \mathbf{k}/m$ to spatial coordinates in the detector *xy*-plane: $\Delta \mathbf{r} = T_f \Delta \mathbf{v}$, where *m* is the mass of a ^{4}He* atom.
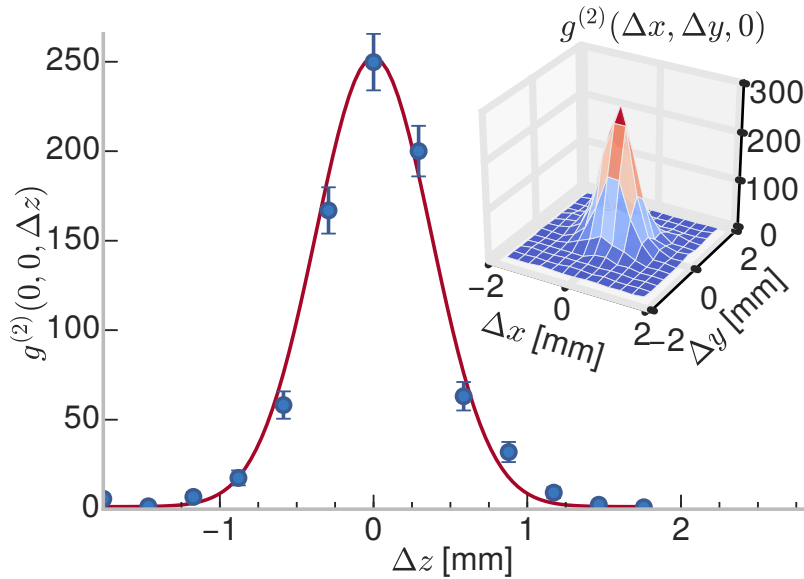

Figure 5.13: Cross-correlation function. The main plot shows $g^{(2)}(0,0,\Delta z)$ as a function of vertical coordinate only. The solid line is a Gaussian fit, which has an rms width $\sigma_z = 0.37$ mm, corresponding to the correlation length. Error bars show the statistical error over the 54,473 experimental runs. The inset shows $g^{(2)}(\Delta x, \Delta y, 0)$ for the experimental data.

We find that the rms widths of the $g^{(2)}$ are approximately constant across all diffraction orders. Note that the correlation lengths we measure are actually a convolution of real correlation length with the ~120 µm detector resolution.

The error estimate in the numerical evaluation of $g^{(2)}$ can be expressed as a standard deviation of the atom count frequencies (which represent the numerator of Eq. 5.14) nor-

malised to the same denominator. The error bars on Fig. 5.13 represent a 2σ confidence interval. The data used to produce Fig. 5.13 was taken from 54,473 experimental runs under identical experimental conditions to those used to produce the ghost image but without the object mask in front of the detector, since the mask blocks a large portion of the halos.

5.7 $g^{(3)}$.

5.7.1 Cauchy-Schwarz violation.

which is a violation of the simplest formulation of the Cauchy-Schwarz inequality [**?**] for our system, which dictates that classically we would be restricted to

$$g^{(2)}_{\text{BB}}(0) \leq g^{(2)}_{\text{CL}}(0). \tag{5.15}$$